IEEE Open Journal of
Antennas and Propagation

Received 24 May 2020; revised 22 June 2020; accepted 1 July 2020. Date of publication 7 July 2020; date of current version 29 July 2020.

Digital Object Identifier 10.1109/OJAP.2020.3007728

Characteristic-Mode-Based Design of Planar In-Band Full-Duplex Antennas

QIANYI LI (Student Member, IEEE), AND TING-YEN SHIH (Member, IEEE)

Department of Electrical and Computer Engineering, University of Idaho, Moscow, ID 83844, USA

CORRESPONDING AUTHOR: T.-Y. SHIH (e-mail: tshih@uidaho.edu)

ABSTRACT In-band full-duplex radios demand simultaneous transmit and receive (STAR) antennas with high isolation, compact and ultra-low profiles, and simple feed networks. Current state-of-the-art designs rarely meet all of these requirements at the same time. In this paper, we present a characteristic-mode-based design approach to achieve high isolation using compact fully-planar STAR antennas with a simple feed structure. The proposed method utilizes two characteristic modes of a conducting object as transmit and receive chains to achieve high isolation without a complicated self-interference cancellation circuit. The design example in this work is fully-planar, and it has a physical height of 1.6 mm. The measured -10 dB overlapped $|S_{11}|$ and $|S_{22}|$ fractional bandwidth of this STAR antenna is 2.5% and the measured isolation between the transmit and receive ports is greater than 30 dB over the entire frequency band of operation.

INDEX TERMS Characteristic mode theory, in-band full-duplex antennas, in-band full-duplex radios, low-profile antennas, and simultaneous transmit and receive (STAR) antennas.

I. INTRODUCTION

IN-BAND full-duplex (IBFD) wireless communication systems can simultaneously transmit and receive signals using the same frequency channel and have significant advantages over frequency division duplex (FDD) systems and time division duplex (TDD) systems as they can, theoretically, double the spectral efficiency [1]–[4]. IBFD systems are in high demand in both military and civilian applications such as full-duplex radars, cognitive radio (CR) networks, simultaneous wireless power transmission, and 5G wireless communication systems [4]. To achieve IBFD, a high isolation between the transmit (TX) and receive (RX) chains is needed. In some IBFD applications, it is required that the simultaneous transmit and receive (STAR) antenna(s) and all the cancellation circuits in the wireless system contribute to a combined 110 dB–120 dB isolation [5], [6]. IBFD wireless radios may not always require the TX and RX antennas to possess the same polarization; however, ultra-low-profile and compact designs with simple feed networks are in demand.

The enhancement of isolation for IBFD radios can be realized in the antenna propagation, analog, and/or digital domains. In the antenna propagation domain, the major goal of passive isolation techniques is to minimize the direct coupling between the TX and RX channels in the near-field region. The existing techniques can be approximately categorized into the following classes [7]: a) separation in physical space, b) dual polarization, c) near-field cancellation, d) passive decoupling networks, e) surface treatments, and f) characteristic modes, as shown in Figure 1:

a) Separation in physical space: The main idea of this method is to increase the distance between the TX and RX antennas, as the path loss increases with it. In Figure 1(a), two antennas are separated by a distance, D. The isolation between the TX and RX channels increases when D increases [8]. In practical designs, D is limited by the space available for antenna placement.
b) Dual polarization: This method utilizes antennas that operate with orthogonal polarizations (i.e., polarization diversity), as shown in Figure 1(b). The isolation between the TX and RX channels can be extremely high. In some designs, this concept was realized using two linear orthogonal polarizations created by an antenna fed by a hybrid ring coupler of a size comparable to the antenna [9], [10], while in others, it was realized using two circular orthogonal polarizations (e.g., right- and left-hand circular polarizations) created by four patches [11] or two spiral antennas [12]. The isolation of this kind of designs is typically limited

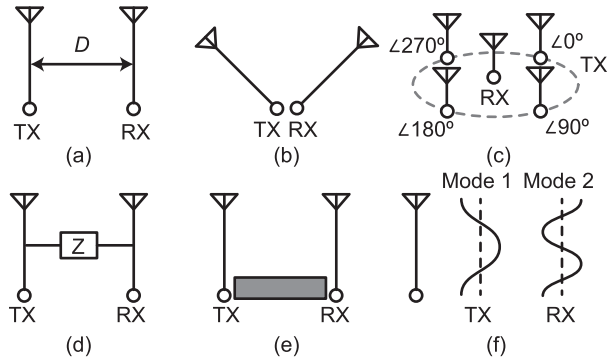

FIGURE 1. Passive isolation techniques in the antenna propagation domain. (a) Separation in physical space. (b) Dual polarization. (c) Near-field cancellation. (d) Passive decoupling networks. (e) Surface treatments. (f) Characteristic modes.

by the imperfections of the fabricated antennas and the feed networks, and it is very sensitive to the degree of symmetry of the antennas and feed structures.

c) Near-field cancellation: In this method, when TX signals from the designed phased array combine in space, they create near-field nulls where the RX antenna(s) is placed, as shown in Figure 1(c). The number of TX (or RX) array elements could be two [13]–[15] or more [16]–[19]. When there are two array elements, although high isolation can be achieved, the far-field gain patterns of the TX phased array are usually different from the ones of the RX antenna. High isolation and resembling radiation patterns can be achieved by using a circular array. However, this technique requires multiple antenna elements, phase shifters, and/or complicated feed networks.

d) Passive decoupling networks: The direct coupling between the TX and RX antennas can be canceled out by a passive decoupling network composed of resistors, inductors and capacitors, as shown in Figure 1(d). This technique is not capable of reducing the reflected path signals due to the fixed components in the network [20]. Decoupling networks are usually narrow-band or have low transmission efficiencies.

e) Surface treatments: The surface currents and surface waves between the TX and RX antennas can be suppressed by absorber materials or engineered materials (e.g., high impedance surfaces, electromagnetic band-gap structures, wavetraps), as shown in Figure 1(e). An example of this method is presented in [21], where a wavetrap structure, a resonant structure that minimizes the magnetic fields between antennas and reduces surface currents, is employed. This method requires modification of the ground plane to form a periodic structure. It is difficult to employ this method when there is limited space for the antenna. The bandwidth of this kind of designs is usually very narrow.

f) Characteristic modes: Characteristic-mode-based techniques (Figure 1(f)) have been applied to decrease the coupling between the antennas of multiple-input-multiple-output (MIMO) systems by introducing diversity in the radiation patterns [22]– [25]. In such MIMO applications, polarization is usually not considered a major design goal and pattern diversity is preferred; whereas in in-band-full-duplex (IBFD) applications, polarization is an important characteristic while pattern diversity should be minimized in order to transmit and receive signals in the same direction(s). The characteristic mode theory has also been employed to decouple the TX and RX ports in a full-duplex system [26]. This method can be used to excite an orthogonal set of modal currents/patterns of a single metallic object with either the same or different polarization. It could offer high isolation and compactness (i.e., it utilizes space more efficiently). However, to take full advantage of this method, a systematic design process still needs to be established.

In this paper, we present a step-by-step method to comprehensively utilize the characteristic mode method for designing fully-planar STAR antennas with different (see Section III) or the same polarization (see Appendix A) for in-band-full-duplex (IBFD) wireless communication systems. Specifically, two major characteristic modes of a metallic object are excited to serve as TX and RX modes. A STAR antenna was fabricated and measured to illustrate the proposed method. The design example employs distributed elements (e.g., open stubs) as feed structure. The electrical size of the antenna with the feed structure is $0.51\lambda \times 0.51\lambda \times 0.01\lambda$, where λ is the wavelength at the lowest frequency of operation, 2.47 GHz (determined by the measurement results). The physical height of the antenna is 1.6 mm. The measured -10 dB overlapped $|S_{11}|$ and $|S_{22}|$ fractional bandwidth (i.e., where $|S_{11}|$ and $|S_{22}|$ are both below -10 dB) of the antenna is 2.5%. The antenna maintains a measured isolation greater than 30 dB, over the entire band of operation. In Appendix B, a method is provided for tuning the TX-RX isolation by examining and adjusting the weighting coefficients of the excited modes. Please note that, since our main intention in this paper is to present a systematic method for designing compact planar STAR antennas with high isolation and simple feed structures using the characteristic mode theory, as opposed to presenting ready-for-launch products for IBFD applications, the design example in this paper is simply meant to serve as a proof-of-concept prototype.

II. CHARACTERISTIC-MODE-BASED DESIGN STRATEGY

The characteristic mode theory can be used to analyze the intrinsic modes of an arbitrarily metallic object. As these intrinsic characteristic modes are an orthogonal set of eigencurrents and fields scattered or radiated by the object, any two characteristic modes from the set are orthogonal to each other [27]. In other words, the isolation between any two characteristic modes is theoretically infinite. We utilize this orthogonality to design STAR antennas with high isolation.

The selection of characteristic modes is based on the antenna design goals, such as bandwidth, isolation, polarization, and radiation characteristics. For IBFD wireless communication systems, the top design priority is to suppress the self-interference (i.e., increase the TX-RX isolation) from the transmitter to the receiver. To achieve this, one characteristic mode of the antenna is selected for transmitting and another for receiving. In IBFD applications, polarizations are usually not the top design consideration. The proposed characteristic-mode-based approach can be used to design STAR antennas where the TX and RX modes possess either different or the same polarization(s). This can be achieved by simply choosing characteristic modes with different or the same polarization(s) for TX and RX, as presented in our design examples in Section III and Appendix A, respectively.

To excite the desired modes and use them for TX and RX, their associated modal currents (i.e., eigen-currents) need to be calculated. The modal current, $\mathbf{J}_n$, of each mode of a metallic object can be determined from the generalized eigen-value equation [27]:

$$[X](\mathbf{J}_n) = \lambda_n[R](\mathbf{J}_n) \tag{1}$$

where λ_n is the eigenvalue associated with the n^{th} eigen-current $\mathbf{J}_n$, and $[R]$ and $[X]$ are the real and imaginary parts of the impedance matrix of the electric field integral equation (EFIE), respectively. A parameter to measure the potential radiation contribution of each characteristic mode is the modal significance (MS) [28]. Assuming that a characteristic mode is fully excited by an external source, its MS can be defined as

$$\text{MS} = \left| \frac{1}{1 + j\lambda_n} \right| \tag{2}$$

where λ_n is the eigenvalue of the n^{th} eigen-current. When the MS value of a mode is equal to or greater than 0.707, that mode is considered significant. When the MS value of a mode is 1, that mode is considered resonant. The closer the value of MS is to 1, the more effectively the associated mode contributes to radiation (i.e., the higher the MS, the easier it is to excite the mode). Note that the MS of a mode increases (eigenvalue decreases) when the product of ka increases, where k is the wave number and a is the radius of the smallest sphere that encloses the antenna [29].

A flow chart of the proposed characteristic-mode-based design process is shown in Figure 2. It starts with examining the arbitrary conducting object using the characteristic mode theory. Subsequently, the modes are selected based on the desired characteristics. To deliver energy from sources to the object and excite the modes, coupling elements are designed and strategically placed on the object. For example, inductive (capacitive) coupling elements should be placed where the modal currents are maximal (minimal) [28], [30]. The combined structure of the initial object and the coupling elements should be re-examined using the characteristic mode theory as the characteristic modes of the combined structure could be very different from the intrinsic modes of the initial object. If that is the case, the coupling elements need to be redesigned. The currents excited by the coupling elements are usually a combination of modal currents (i.e., not a single pure mode). If the weighting of the desired mode is low, the coupling elements need to be re-designed. If the input impedance is not equal to 50 Ω, a matching network composed of lumped and/or distributed elements is needed. Finally, the prototype can be fabricated and measured.

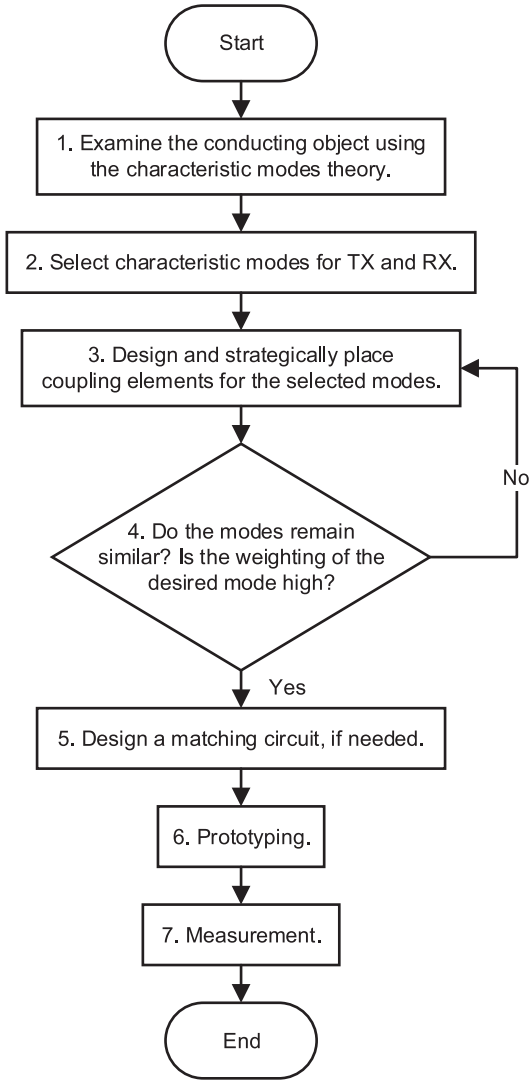

FIGURE 2. The flow chart of the characteristic-mode-based design strategy.

III. ANTENNA DESIGN

Due to the low-profile requirement of most IBFD applications, we started our design from a planar metallic square with the size of 50 mm × 50 mm. The characteristic mode analysis of the square was carried out at 2.4 GHz using Altair FEKO. The normalized modal currents and field patterns of the first eight characteristic modes of the square are shown in Figure 3. FEKO numbers the characteristic modes according to their modal significance values and from low

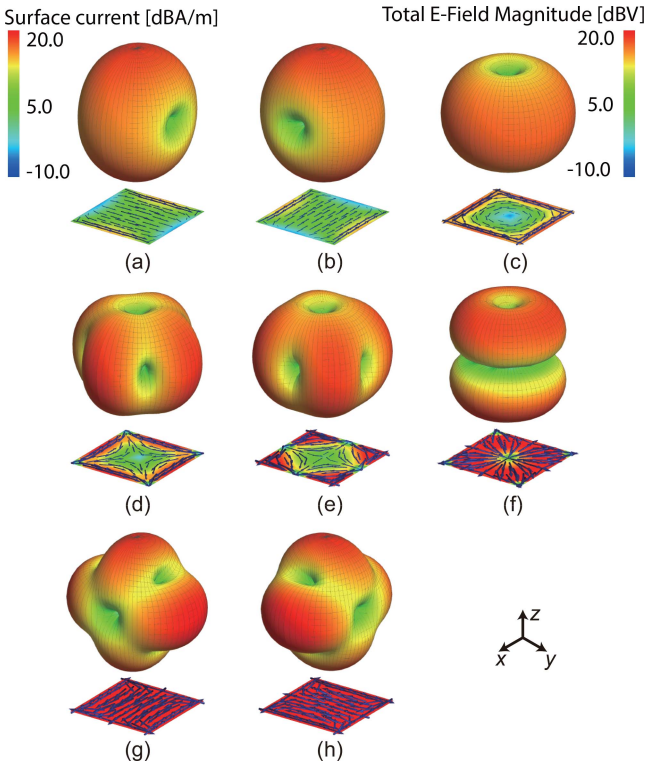

FIGURE 3. Normalized modal currents and field patterns of the first eight characteristic modes of the metallic square at 2.4 GHz: (a) Mode 1, (b) mode 2, (c) mode 3, (d) mode 4, (e) mode 5, (f) mode 6, (g) mode 7, and (h) mode 8.

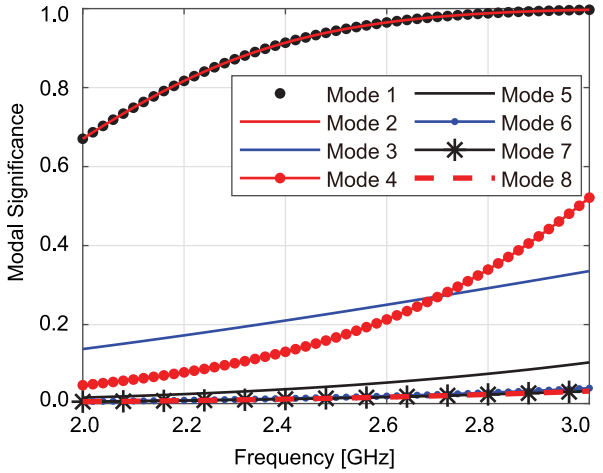

FIGURE 4. Modal significance of the first eight characteristic modes of the metallic square.

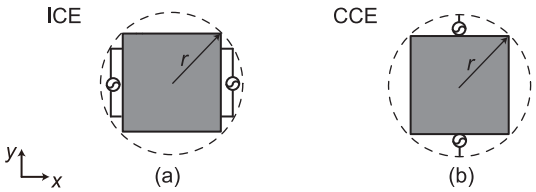

FIGURE 5. Placement of coupling elements to excite mode 1: (a) Inductive coupling elements (ICEs) and (b) capacitive coupling elements (CCEs). Note that, to excite mode 2, the elements should be rotated 90°.

frequency to high frequency. Modes 1 and 2 (Figure 3(a) and (b)) are dipole modes aligned along the $\hat{x}$ and $\hat{y}$ axes, respectively. The maximum radiations of these two modes are both towards zenith. The modal significance values of the first eight modes are calculated from 2 GHz to 3 GHz, as shown in Figure 4. As can be observed, modes 1 and 2 are significant (MS $>$ 0.707) throughout the entire examined frequency band. The broadside radiation and high modal significance properties make modes 1 and 2 good candidates for IBFD compared to the rest of the modes. To demonstrate the proposed method, modes 1 and 2 are used to design a STAR antenna with different polarizations. However, the concepts are equally applicable to the design of STAR antennas with the same polarization (see Appendix A).

To excite the desired modes, inductive coupling elements (ICEs) or capacitive coupling elements (CCEs) can be placed where the modal currents are maximum or minimum, respectively. Typical coupling elements include half loops (used as ICEs) and monopoles (used as CCEs). As can be observed in Figure 5, without increasing the maximum linear dimension of the square STAR antenna (i.e., staying within the same Chu's sphere [31] with the radius of r), the available space can only accommodate very short monopole CCEs while much larger half loop ICEs can be accomodated. Larger coupling elements within the same Chu's sphere have a higher excitation efficiency than smaller ones since they utilize the space more efficiently. This makes ICEs more preferable for our square-shaped antenna. Also note that the pair of CCEs in Figure 5 needs to be fed with the same magnitude and 180° phase difference. This increases the complexity of the feed network due to the need of a phase shifter, a hybrid coupler, or a transformer. In addition, when using top-loaded monopoles as CCEs, the antenna's cross-polarization level increases, which results in poor TX-RX isolation. Hence, we employ half loops which are fed with the same magnitudes and phases as coupling elements in this design.

To achieve high-purity mode excitation, not only the placement of the half loops needs to be considered, but also the current distributions on the half loops. While placing the feed at the edge of the half loops produces asymmetrical current distributions (Figure 6(a)), symmetrical current distribution can be achieved by placing the feed at the center of the half loops, as shown in Figure 6(b). Since the desired modes are both symmetrical, it is preferable that the currents on the half loops also be symmetrical. However, in practice, the feed line is a microstrip line, which is an unbalanced structure. Thus, a balun or a transition is required. To keep the feed structure simple and balanced, a two-arm structure that can be considered as the 2-D version of a shielded loop was designed to serve as transition (Figure 6(c)). Using this coupling element, simple planar metallic structures can be easily excited, and no cutting of the metallic structure is required.

To prevent being affected by the tolerance of commercial lumped elements and to reduce the cost, it is often preferred

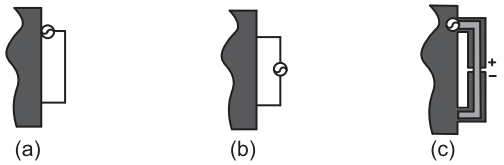

FIGURE 6. Feeding of the half loops: (a) Unbalanced feed, (b) balanced feed, and (c) two-arm balanced feed. Depending on the desired port impedance, the end of the microstrip line in (c) can be terminated with open, short, or other types of loads.

TABLE 1. Physical dimensions of the antenna.

Parameter	Dimension [mm]	Parameter	Dimension [mm]
L_1	100.0	D_1	5.00
L_2	50.00	D_2	6.00
L_3	5.10	D_3	3.00
L_4	5.20	W_1	4.00
L_5	7.50	W_2	1.00
L_6	11.45	W_3	3.00
G	1.10		

that the matching circuit be incorporated into the antenna (e.g., using a distributed-element-based matching circuit). Hence, the feed structure of the square antenna was designed using distributed elements and printed on the top metal layer of a PCB, as shown in Figure 7 (a). The gaps between the two-arm structures in Figure 7(b) are part of the transition between the unbalanced microstrip lines and the balanced arms. These gaps can be modeled as capacitors. The L-shaped arms in Figure 7(a) are used to transform the real part of the input impedance of each port to around 100 Ω. The imaginary part of the input impedance of each port can be canceled out by the added open stubs (Figure 7(a)). The input impedances of ports 1, 2, 3 and 4 are $96.7 - j3.87$ (Ω), $106 + j4.66$ (Ω), $97.5 - j9.73$ (Ω) and $104 + j9.97$ (Ω), respectively. Ports 1 and 2 (ports 3 and 4) are connected to the TX port (RX port) using a tee adaptor, as shown in Figure 7(c). The combined impedance of the TX and RX ports are approximately 50 Ω at the desired frequency. The detailed physical dimensions of the antenna are listed in Table 1. The antenna with the feed structure was examined using the characteristic mode analysis. As can be observed by comparing Figures 3 and 8, modes 1 and 2 of this structure are similar to the intrinsic modes 1 and 2 of the metallic square. The modal significance of these two modes are significant (MS $>$ 0.707) from 2 GHz to 3 GHz (Figure 9). In this design example, mode 1 is used as TX and mode 2 as RX.

As one of the major goals of STAR antenna design is to achieve high isolation, it is desired that the excited modes be as pure as possible. Theoretically, due to the orthogonality of the characteristic modes, the isolation between any two modes is infinite when only one characteristic mode is excited by each excitation. Practically, any feed structure placed on the metallic object excites a series of characteristic modes with different weightings. The purity of the excited modes determines the level of isolation between excitations (Appendix B). To quantify the purity, the weighting coefficients of the modes can be examined. In the

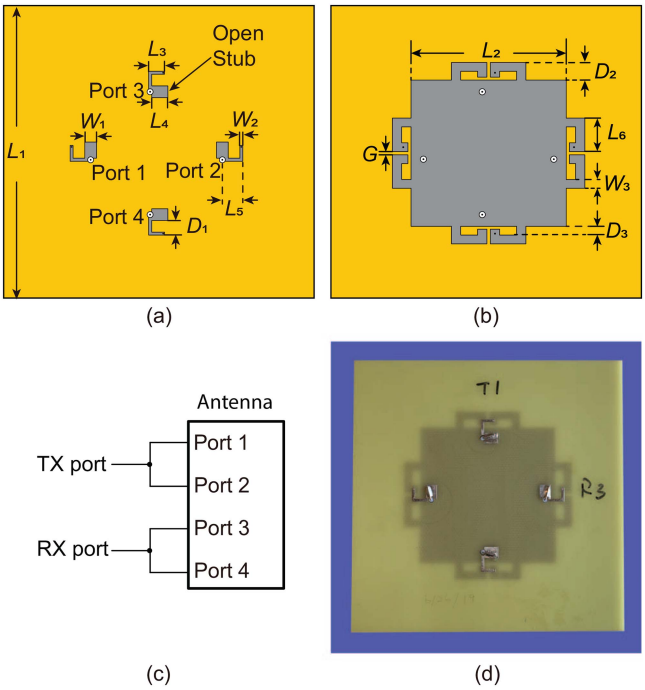

FIGURE 7. The antenna with the feed structures and the distributed matching circuits: (a) Top layer, (b) bottom layer, (c) schematic of the external connections, and (d) top view of the antenna prototype.

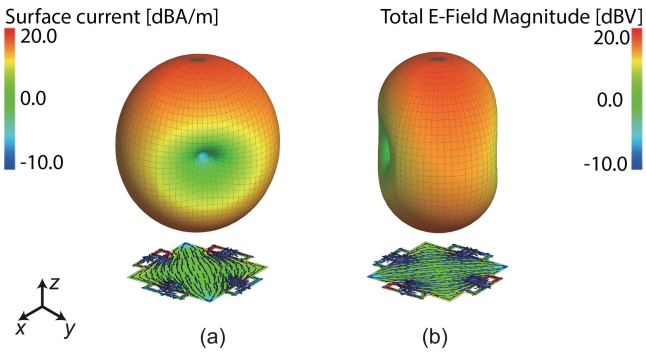

FIGURE 8. Normalized modal currents and field patterns of the first two characteristic modes of the antenna at 2.4 GHz: (a) Mode 1 and (b) mode 2.

characteristic mode theory, the total current on the surface of a conducting body, $\mathbf{J}$, can be expanded to a basis set of modal currents (i.e., eigen-currents), $\mathbf{J}_n$, with the associated weighting coefficience of the n^{th} modal current, α_n:

$$\mathbf{J} = \sum_n \alpha_n \mathbf{J}_n = \sum_n \frac{V_n^i \mathbf{J}_n}{1 + j\lambda_n} \tag{3}$$

where V_n^i is the modal excitation coefficient. It is defined as [27]:

$$V_n^i = \left\langle J_n, E^i \right\rangle = \oint_S \mathbf{J}_n \cdot \mathbf{E}^i ds. \tag{4}$$

The modal excitation coefficient (V_n^i) accounts for how the positions, magnitudes, and phases of the excitation affect the contribution of each characteristic mode to the total current, $\mathbf{J}$. Consequently, V_n^i reflects the coupling between the excitation ($\mathbf{E}^i$) and the n^{th} eigen-current ($\mathbf{J}_n$), and describes how

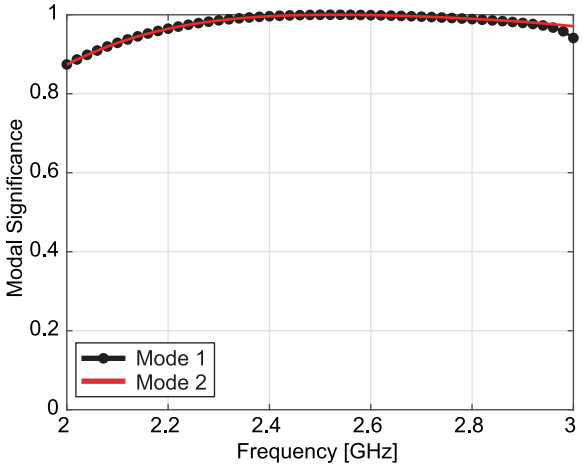

FIGURE 9. Simulated modal significance (MS) of mode 1 and mode 2 of the antenna.

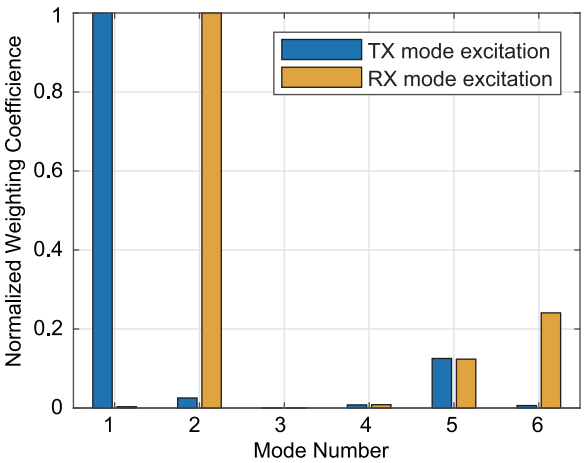

FIGURE 10. Normalized weighting coefficients of the modes excited by the TX and RX ports.

TABLE 2. Comparison of simultaneous transmit and receive (STAR) antennas.

Reference	Size[1]	Isolation[2]	Gain
[10]	$0.46\lambda \times 0.78\lambda \times 0.01\lambda$	40 dB	3.7 dBi
[11]	$2.20\lambda \times 2.20\lambda \times 0.07\lambda$	40 dB	8.7 dBi
[17]	$0.77\lambda \times 0.77\lambda \times 0.24\lambda$	40 dB	5.5 dBi
[20]	$0.52\lambda \times 0.17\lambda \times 0.01\lambda$	30 dB	-1.6 dBi
[21]	$1.28\lambda \times 1.54\lambda \times 0.21\lambda$	63 dB	10.5 dBi
This work	$0.51\lambda \times 0.51\lambda \times 0.01\lambda$	30 dB	3.0 dBi

[1] Electrical sizes were calculated at the lowest frequency of operation.
[2] The lowest isolation within the operating frequency band.

well a particular mode is excited by the feed. The normalized weighting coefficients of the modes excited by the TX and RX ports are shown in Figure 10. As can be observed, when the antenna is excited by the TX port, mode 1 is dominant (has the highest weighting coefficient). On the other hand, mode 2 is dominant when the metallic square is excited by the RX port.

IV. RESULTS

The prototype of this design was fabricated on a two-layer PCB (FR-4 substrate, $\epsilon_r = 4.4$, $h = 1.6$ mm and

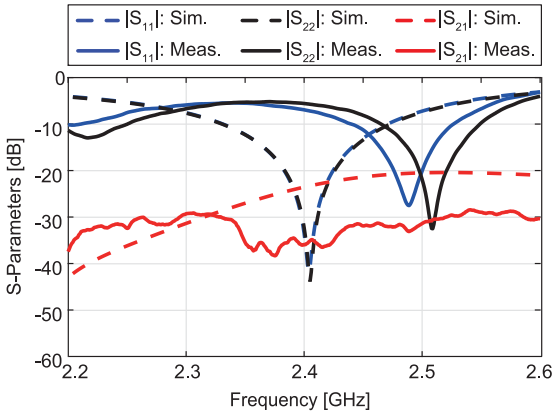

FIGURE 11. Simulated and measured S-parameters of the antenna.

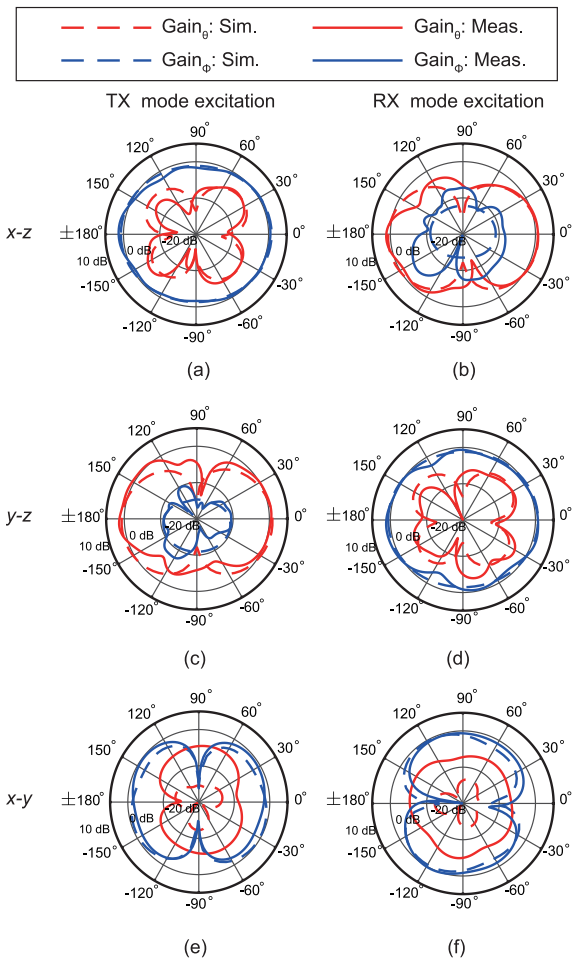

FIGURE 12. The simulated and measured normalized gain patterns of the antenna at 2.4 GHz and 2.5 GHz, respectively: TX mode in the (a) $x-z$, (c) $y-z$, and (e) $x-y$ planes; RX mode in the (b) $x-z$, (d) $y-z$, and (f) $x-y$ planes.

tan $\delta = 0.02$), as shown in Figure 7(d). The simulated and measured S-parameters of the antenna are shown in Figure 11. The simulations were performed using Altair FEKO. The simulated and measured -10 dB overlapped $|S_{11}|$ and $|S_{22}|$ fractional impedance bandwidths are 5.7% and 2.5%, respectively. Note that these are overlapped fractional

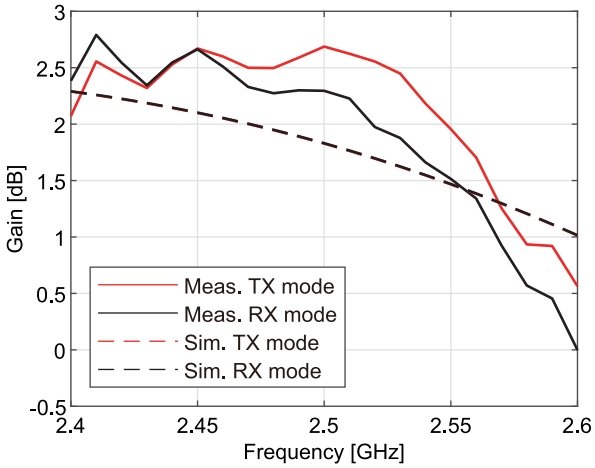

FIGURE 13. The simulated and measured realized gain of the antenna in the *z* direction.

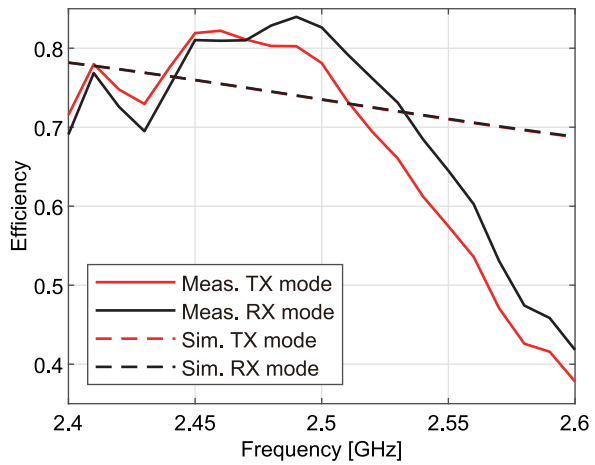

FIGURE 14. The simulated and measured efficiencies of the antenna.

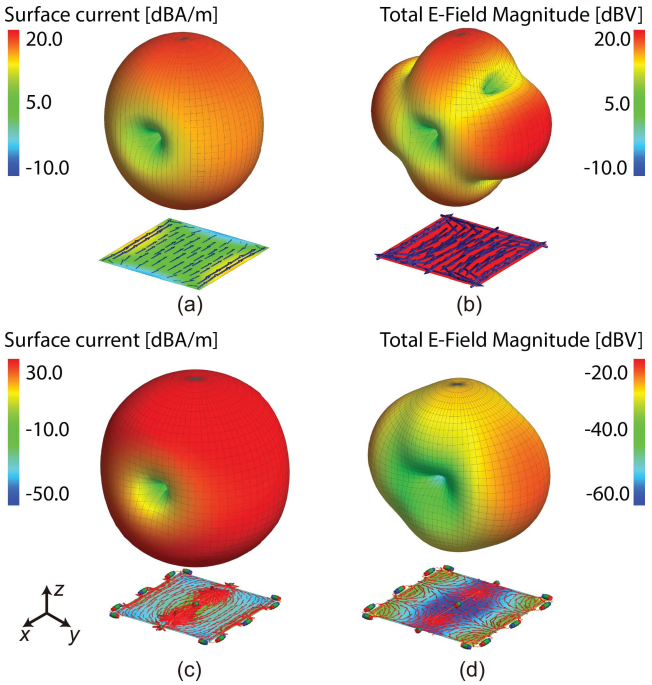

FIGURE 15. Normalized currents and radiation patterns at 2.4 GHz: (a) Mode 2 and (b) mode 7 of the square, and (c) TX excitation and (d) RX excitation.

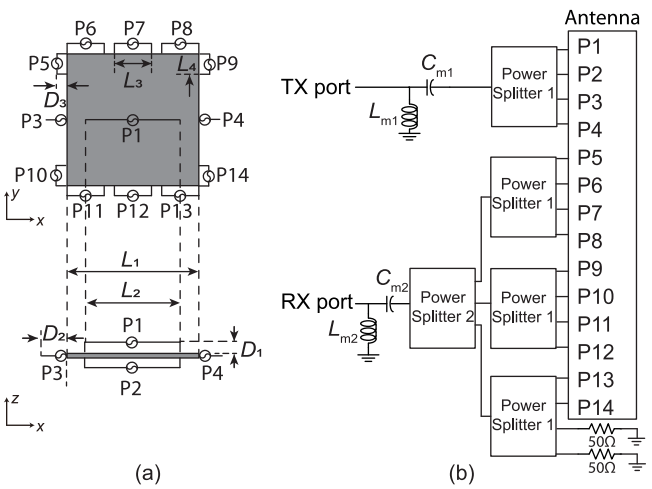

FIGURE 16. (a) The feed scheme and (b) the detailed feed network of the STAR antenna with the same polarization. $L_1 = 50$ mm, $L_2 = 30$ mm, $L_3 = 10$ mm, $L_4 = 4$ mm, $D_1 = 1$ mm, $D_2 = D_3 = 2$ mm, $L_{m1} = 1.22$ nH, $C_{m1} = 0.688$ pF, $L_{m2} = 2.27$ nH, and $C_{m2} = 1.06$ pF. Power Splitter 1 is a 4-way power splitter (Mini-Circuits BP4U1+) and Power Splitter 2 is a 3-way power splitter (Mini-Circuits SEPS-3-33+).

bandwidths of the TX and RX modes (i.e., where $|S_{11}|$ and $|S_{22}|$ are both below -10 dB). The difference between the simulated and measured overlapped bandwidth is caused by the misalignment of the center frequencies of the measured S_{11} and S_{22}. The frequency shift between the simulation and measurement is mainly caused by a small phase imbalance between the four coaxial cables used in the measurement. The simulated and measured $|S_{21}|$ are below -21 dB and -30 dB, respectively. The discrepancy between the simulated and measured isolation (isolation $= -|S_{21}|$) is caused by fabrication error and the phase imbalance of the cables. This can be improved by employing high precision PCB technology or focused ion beam (FIB) technology for fabrication. The excitation of the TX and RX modes using practical feed structures resulted in minor impurity of the excited modes. As a result, unwanted modes like mode 5 and mode 6 in Figure 10 are excited along with the desired modes 1 and 2. The isolation between TX and RX can be enhanced by redesigning the coupling elements to strengthen the excitation of the desired modes and suppress the unwanted modes, as demonstrated in Appendix B.

The radiation parameters of the fabricated prototype were measured using a multiprobe spherical near-field system, MVG StarLab. The simulated and measured normalized gain patterns of the antenna are shown in the *x*-*z*, *y*-*z*, and *x*-*y* planes in Figure 12. As can be observed, the simulation and measurement results are in good agreement. The simulated and measured realized gain and efficiencies of the antenna

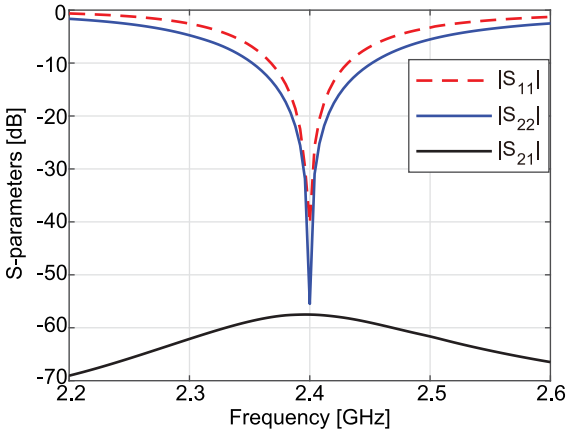

FIGURE 17. Simulated S-parameters of the STAR antenna with the same polarization.

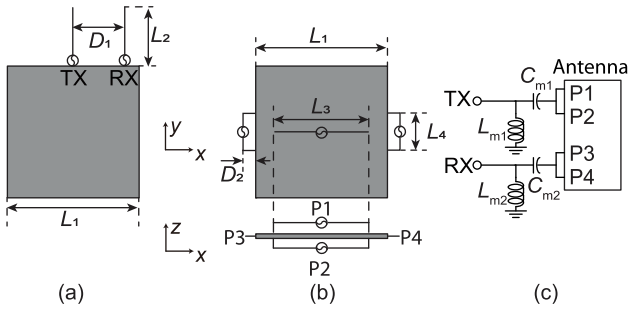

FIGURE 18. (a) Low isolation case. (b) High isolation case and (c) its feed network. $L_1 = 50$ mm, $L_2 = 20$ mm, $L_3 = 30$ mm, $L_4 = 10$ mm, $D_1 = 20$ mm, $D_2 = 5$ mm, $L_{m1} = 2.77$ nH, $C_{m1} = 0.151$ pF, $L_{m2} = 1.51$ nH, $C_{m2} = 0.378$ pF.

are shown in Figure 13 and Figure 14, respectively. As can be observed, the simulated realized gains of both the TX and RX modes are 2.3 dBi at 2.4 GHz, while the measured realized gains of the TX and RX modes are 2.7 dBi and 2.3 dBi, respectively, at 2.5 GHz. The simulated efficiencies of the TX and RX modes are both 78% at 2.4 GHz and the measured efficiencies of the TX and RX modes are 78% and 83%, respectively, at 2.5 GHz. Note that the center frequency of the design is 2.4 GHz in the simulations. However, as aforementioned, a frequency shift occurred in the measurements due to the fabrication error and the phase imbalance of the cables, resulting in a center frequency of 2.5 GHz. Table 2 compares the performance of the example design with STAR antennas designed using other methods. The STAR antenna from this work is compact and has an ultra-low profile, high isolation, and a simple feed structure compared to the others.

V. CONCLUSION

In this paper, a characteristic-mode-based simultaneous transmit and receive (STAR) antenna design approach was proposed for in-band full-duplex radios. A systematic design procedure was presented and a design example was discussed. In the design example, two characteristic modes of a compact planar square were excited, one for transmitting and the other for receiving. A prototype of the design example was fabricated and measured. The physical height of the prototype is 1.6 mm and the electrical size is $0.51\lambda \times 0.51\lambda \times 0.01\lambda$, where λ is the wavelength at the lowest frequency of operation. The measured -10 dB overlapped $|S_{11}|$ and $|S_{22}|$ fractional impedance bandwidth of the design is 2.5%. Throughout the entire frequency band of operation, the measured isolation of the design example remains greater than 30 dB.

APPENDIX A

SIMULTANEOUS TRANSMIT AND RECEIVE (STAR) ANTENNAS WITH THE SAME POLARIZATION

The characteristic mode theory approach can also be used to design STAR antennas where the transmit (TX) and receive (RX) modes possess the same polarization. This can be achieved by employing characteristic modes with the same polarization as TX and RX. Mode 2 and mode 7 of the planar square used in Section III have the same polarization (Figure 15(a) and (b)), and are used in this example. Figure 16 presents the feed scheme and the detailed feed network of the STAR antenna with the same polarization. To excite mode 2 (TX mode), two ICE ports (P1, P2) and two CCE ports (P3, P4) are employed and combined with power dividers. To excite mode 7 (RX mode), ten ICE ports (P5–P14) are used and combined with power dividers. The polarities of P7 and P12 are different from the other ports. This excitation method is only one of the many potential ways that can be used to excite the same-polarized modes on the planer metallic square. The design of the feed structure of same-polarized STAR antennas is generally more complicated compared with different-polarized antennas. It is common that many ports are needed to excite same-polarized modes in STAR antennas. For example, eight ports and one port are used for the TX and RX modes, respectively, to achieve same-polarized radiation in [16]. We anticipate that if the same-polarized antenna design example in Appendix A is to be commercialized, multi-way power splitters can be used to simplify the feed structure and a mode that requires fewer ports can be used.

The simulated normalized current and radiation patterns excited by the TX and RX ports of this antenna are shown in Figure 15(c) and (d). As can be observed, the excited TX and RX modes are very similar to the characteristic modes 2 and 7. The simulated S-parameters of this example are shown in Figure 17. The simulated -10 dB overlapped $|S_{11}|$ and $|S_{22}|$ fractional impedance bandwidth is 2.65%. The simulated isolation of this design example is greater than 58 dB throughout the entire frequency band of operation.

APPENDIX B

EFFECT OF CORRELATION BETWEEN TWO EXCITED MODE SERIES ON ISOLATION

To demonstrate how the correlation between two excited mode series affects isolation, we employ two different scenarios to excite a desired set of TX and RX modes (characteristic modes 1 and 2 of the metallic square from

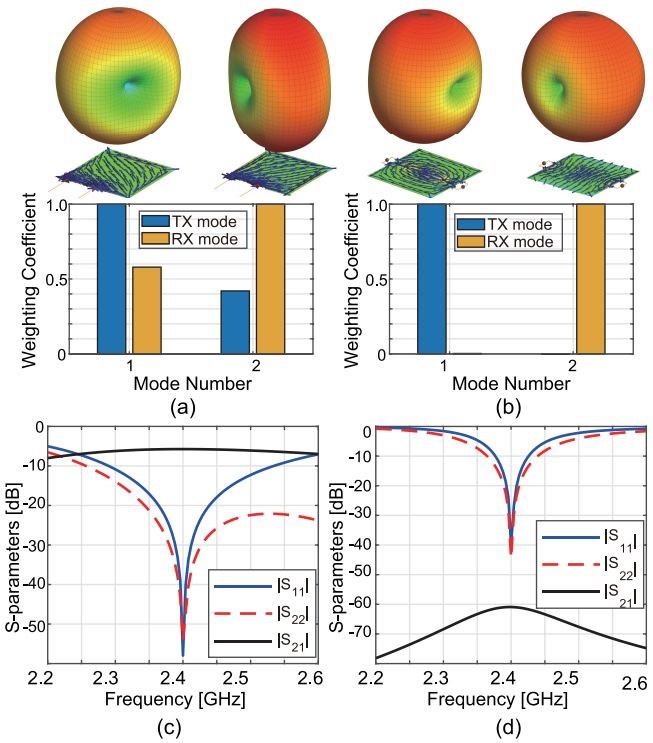

FIGURE 19. Normalized weighting coefficient of (a) scenario 1 and (b) scenario 2 at 2.4 GHz; S-parameters of (c) scenario 1 and (d) scenario 2.

Section III, as shown in Figure 3(a) and (b)). Figure 18 shows the two excitation scenarios that are used to excite the desired modes. Figure 18(a) is a low isolation case and Figure 18(b) is a high isolation case. Figure 19 presents the normalized weighting coefficient and S-parameters of the two scenarios. As can be observed, in scenario 1, mode 1 is the dominant mode from TX excitation, but mode 2 which is used for RX is also excited (Figure 19(a)), resulting in the poor isolation ($<$ 10 dB) between TX and RX ports (Figure 19(c)). On the contrary, scenario 2 provides a much higher isolation ($>$ 60 dB, Figure 19(d)) because this structure can efficiently and purely excite the desired TX and RX modes, as shown in Figure 19(b).

ACKNOWLEDGMENT

The authors would like to thank Dr. Nader Behdad and Mr. Ruyu Ma from the University of Wisconsin–Madison for their help with the radiation pattern measurements.

REFERENCES

[1] S. Chen, M. Beach, and J. McGeehan, "Division-free duplex for wireless applications," *Electron. Lett.*, vol. 34, no. 2, pp. 147–148, Jan. 1998.

[2] Y. S. Choi and H. Shirani-Mehr, "Simultaneous transmission and reception: Algorithm, design and system level performance," *IEEE Trans. Wireless Commun.*, vol. 12, no. 12, pp. 5992–6010, Dec. 2013.

[3] A. Sabharwal, P. Schniter, D. Guo, D. W. Bliss, S. Rangarajan, and R. Wichman, "In-band full-duplex wireless: Challenges and opportunities," *IEEE J. Sel. Areas Commun.*, vol. 32, no. 9, pp. 1637–1652, Sep. 2014.

[4] D. Kim, H. Lee, and D. Hong, "A survey of in-band full-duplex transmission: From the perspective of PHY and MAC layers," *IEEE Commun. Surveys Tuts.*, vol. 17, no. 4, pp. 2017–2046, 4th Quart., 2015.

[5] D. Bharadia, E. McMilin, and S. Katti, "Full duplex radios," in *Proc. ACM SIGCOMM Conf.*, 2013, pp. 375–386. [Online]. Available: http://doi.acm.org/10.1145/2486001.2486033

[6] K. L. Scherer *et al.*, "Simultaneous transmit and receive system architecture with four stages of cancellation," in *Proc. IEEE Int. Symp. Antennas Propag. USNC/URSI Nat. Radio Sci. Meeting*, Jul. 2015, pp. 520–521.

[7] K. E. Kolodziej, B. T. Perry, and J. S. Herd, "In-band full-duplex technology: Techniques and systems survey," *IEEE Trans. Microw. Theory Techn.*, vol. 67, no. 7, pp. 3025–3041, Jul. 2019.

[8] E. Everett, A. Sahai, and A. Sabharwal, "Passive self-interference suppression for full-duplex infrastructure nodes," *IEEE Trans. Wireless Commun.*, vol. 13, no. 2, pp. 680–694, Feb. 2014.

[9] H. Nawaz and I. Tekin, "Three ports microstrip patch antenna with dual linear and linear co-polarisation characteristics," *Electron. Lett.*, vol. 53, no. 8, pp. 518–520, 2017.

[10] H. Nawaz and I. Tekin, "Compact dual-polarised microstrip patch antenna with high interport isolation for 2.5 GHz in-band full-duplex wireless applications," *IET Microw. Antennas Propag.*, vol. 11, no. 7, pp. 976–981, Jun. 2017.

[11] J. Wu, M. Li, and N. Behdad, "A wideband, unidirectional circularly polarized antenna for full-duplex applications," *IEEE Trans. Antennas Propag.*, vol. 66, no. 3, pp. 1559–1563, Mar. 2018.

[12] P. Deo, D. Mirshekar-Syahkal, G. Zheng, A. Pal, and A. Mehta, "Broadband antenna for passive self-interference suppression in full-duplex communications," in *Proc. IEEE Radio Wireless Symp. (RWS)*, Jan. 2018, pp. 243–245.

[13] G. Makar, N. Tran, and T. Karacolak, "A high-isolation monopole array with ring hybrid feeding structure for in-band full-duplex systems," *IEEE Antennas Wireless Propag. Lett.*, vol. 16, pp. 356–359, 2017.

[14] M. A. Elmansouri, A. J. Kee, and D. S. Filipovic, "Wideband antenna array for simultaneous transmit and receive (STAR) applications," *IEEE Antennas Wireless Propag. Lett.*, vol. 16, pp. 1277–1280, 2017.

[15] Z. Chen and Y. P. Zhang, "Mutual coupling between submicrostrip grid arrays on electrically thin substrate," *IEEE Trans. Antennas Propag.*, vol. 66, no. 1, pp. 467–471, Jan. 2018.

[16] K. E. Kolodziej, P. T. Hurst, A. J. Fenn, and L. I. Parad, "Ring array antenna with optimized beamformer for simultaneous transmit and receive," in *Proc. Int. Symp. Antennas Propag.*, Jul. 2012, pp. 1–2.

[17] R. Lian, T.-Y. Shih, Y. Yin, and N. Behdad, "A high-isolation, ultra-wideband simultaneous transmit and receive antenna with monopole-like radiation characteristics," *IEEE Trans. Antennas Propag.*, vol. 66, no. 2, pp. 1002–1007, Feb. 2018.

[18] J. Ha, M. A. Elmansouri, P. V. Prasannakumar, and D. S. Filipovic, "Monostatic co-polarized full-duplex antenna with left- or right-hand circular polarization," *IEEE Trans. Antennas Propag.*, vol. 65, no. 10, pp. 5103–5111, Oct. 2017.

[19] E. A. Etellisi, M. A. Elmansouri, and D. S. Filipović, "Wideband multimode monostatic spiral antenna STAR subsystem," *IEEE Trans. Antennas Propag.*, vol. 65, no. 4, pp. 1845–1854, Apr. 2017.

[20] S. N. Venkatasubramanian, L. Li, A. Lehtovuori, C. Icheln, and K. Haneda, "Impact of using resistive elements for wideband isolation improvement," *IEEE Trans. Antennas Propag.*, vol. 65, no. 1, pp. 52–62, Jan. 2017.

[21] M. Heino, S. N. Venkatasubramanian, C. Icheln, and K. Haneda, "Design of wavetraps for isolation improvement in compact in-band full-duplex relay antennas," *IEEE Trans. Antennas Propag.*, vol. 64, no. 3, pp. 1061–1070, Mar. 2016.

[22] H. Li, B. K. Lau, Z. Ying, and S. He, "Decoupling of multiple antennas in terminals with chassis excitation using polarization diversity, angle diversity and current control," *IEEE Trans. Antennas Propag.*, vol. 60, no. 12, pp. 5947–5957, Dec. 2012.

[23] K. K. Kishor and S. V. Hum, "A two-port chassis-mode MIMO antenna," *IEEE Antennas Wireless Propag. Lett.*, vol. 12, pp. 690–693, 2013.

[24] R. Martens and D. Manteuffel, "Systematic design method of a mobile multiple antenna system using the theory of characteristic modes," *IET Microw. Antennas Propag.*, vol. 8, no. 12, pp. 887–893, Sep. 2014.

[25] H. Li, S. Sun, B. Wang, and F. Wu, "Design of compact single-layer textile MIMO antenna for wearable applications," *IEEE Trans. Antennas Propag.*, vol. 66, no. 6, pp. 3136–3141, Jun. 2018.
[26] Q. Li and T.-Y. Shih, "Design of a characteristic-mode-based fully-planar antenna for indoor in-band full-duplex radios," in *Proc. IEEE Int. Symp. Antennas Propag. USNC URSI Radio Sci. Meeting*, Jul. 2019, pp. 1233–1234.
[27] R. Harrington and J. Mautz, "Theory of characteristic modes for conducting bodies," *IEEE Trans. Antennas Propag.*, vol. 19, no. 5, pp. 622–628, Sep. 1971.
[28] T.-Y. Shih and N. Behdad, "Applications of the characteristic mode theory to antenna design," in *Developments in Antenna Analysis and Synthesis*, R. Mittra, Eds. Stevenage, U.K.: Inst. Eng. Technol., 2018.
[29] J. Chalas, K. Sertel, and J. L. Volakis, "Computation of the Q limits for arbitrary-shaped antennas using characteristic modes," *IEEE Trans. Antennas Propag.*, vol. 64, no. 7, pp. 2637–2647, Jul. 2016.
[30] T.-Y. Shih and N. Behdad, "Bandwidth enhancement of platform-mounted HF antennas using the characteristic mode theory," *IEEE Trans. Antennas Propag.*, vol. 64, no. 7, pp. 2648–2659, Jul. 2016.
[31] L. J. Chu, "Physical limitations of omni-directional antennas," *J. Appl. Phys.*, vol. 19, no. 12, pp. 1163–1175, Dec. 1948.

QIANYI LI (Student Member, IEEE) received the B.S. degree from the University of Electronic Science and Technology of China, Chengdu, China, in 2017. She is currently pursuing the Ph.D. degree in electrical and computer engineering with the University of Idaho, Moscow, ID, USA.

Since 2017, she has been a Research Assistant with the University of Idaho. Her research interests include antennas, RF/microwave circuits, and machine learning applications in electromagnetics.

Ms. Li was a finalist in the Student Paper Competition at the 2019 IEEE AP-S/URSI Symposium. She received the Graduate and Professional Student Association Travel Award from the University of Idaho in 2019, and the College of Engineering Bhanoji Rao Outstanding Graduate Student Award in Electrical Engineering from the University of Idaho in 2020.

TING-YEN SHIH (Member, IEEE) received the Ph.D. degree in electrical engineering from the University of Wisconsin–Madison, USA, in 2017.

Since 2017, he has been an Assistant Professor with the Department of Electrical and Computer Engineering, University of Idaho, Moscow, ID, USA. His research interests include electrically small antennas, antenna arrays, RF/mmWave/THz circuits and systems, bio-electromagnetics, and machine learning applications in electrical engineering.

Dr. Shih received the Young Faculty Award from the U.S. Defense Advanced Research Projects Agency in 2019. He was a recipient of the Best Student Paper Award at the International Conference on Electromagnetic Applications and Compatibility, the Phi Tau Phi Scholarship Award, and the Graduate Academic Achievement Award from the University of Wisconsin–Madison. He was a winner of the international FEKO Student Competition and the National Communication Contests, Taiwan. His graduate student was a finalist in the student paper competition at the IEEE AP-S/URSI Symposium in 2019. He is a member of Sigma Xi and IEEE Eta Kappa Nu.